The valence state and partitioning of iron in the Earth's lowermost mantle

Ryosuke Sinmyo,[1,2] Kei Hirose,[1,3] Shunsuke Muto,[4] Yasuo Ohishi,[5] and Akira Yasuhara[6]

Received 23 December 2010; revised 17 March 2011; accepted 29 March 2011; published 27 July 2011.

[1] While iron occurs predominantly in the form of Fe^{2+} in the Earth's upper mantle and transition zone, Al-bearing $(Mg,Fe)SiO_3$ perovskite (Pv), a primary mineral in the lower mantle, contains a large proportion of ferric iron (Fe^{3+}). It has been demonstrated that such Fe^{3+} strongly affects physical and chemical properties of Pv. On the other hand, the iron substitution mechanism and valence state of iron in postperovskite (PPv) are still unclear. Here we determined the valence state of iron in PPv with changing Al^{3+} content, on the basis of electron energy-loss near-edge structure spectroscopy measurements. The results show that PPv includes a small amount of Fe^{3+}, which is independent from the Al^{3+} content. This indicates that Fe^{3+} in Pv and coexisting metallic iron recombine to form Fe^{2+} upon phase transition from Pv to PPv in pyrolitic mantle. Such Fe^{2+} partitions preferentially into (Mg,Fe)O ferropericlase (Fp), and therefore PPv is depleted in iron compared to Pv. Such a marked change in the valence state of iron and resulting iron depletion in PPv have broad implications for seismic and transport properties in the lowermost mantle. Phase transition from Pv to Fe-poor PPv occurs in a much narrower pressure range than that for a fixed iron content.

Citation: Sinmyo, R., K. Hirose, S. Muto, Y. Ohishi, and A. Yasuhara (2011), The valence state and partitioning of iron in the Earth's lowermost mantle, *J. Geophys. Res.*, *116*, B07205, doi:10.1029/2010JB008179.

1. Introduction

[2] The pyrolitic lower mantle consists predominantly of Al-bearing $(Mg,Fe)SiO_3$ perovskite (Pv) with minor (Mg,Fe)O Fp and $CaSiO_3$-rich perovskite. It is well known that Fe^{3+} content in Pv is strongly controlled by its Al^{3+} content [e.g., *McCammon*, 1997; *Lauterbach et al.*, 2000; *Frost and Langenhorst*, 2002]. The Al-bearing Pv in the pyrolitic mantle thus contains substantial amount of Fe^{3+}, which is formed by a valence disproportionation reaction of Fe^{2+}; $3Fe^{2+} \rightarrow 2Fe^{3+} + Fe^0_{metal}$ [e.g., *McCammon*, 1997, 2005; *Frost et al.*, 2004]. Previous studies have also demonstrated that the presence of Fe^{3+} in Pv strongly changes elastic constants [*Andrault et al.*, 2001; *Catalli et al.*, 2010], electrical/thermal conductivities [*Xu et al.*, 1998; *Goncharov et al.*, 2008], and solubility of water [*Litasov et al.*, 2003]. The valence state of iron also affects Fe partitioning between Pv and Fp [*Wood and Rubie*, 1996; *Frost and Langenhorst*, 2002]. Partitioning of iron into Pv is enhanced in Al-bearing systems, because Fe^{3+} is incorporated primarily in Pv.

[3] On the other hand, the abundance of Fe^{3+} in postperovskite (PPv), a recently discovered main constituent in the lowermost mantle [e.g., *Murakami et al.*, 2004; *Oganov and Ono*, 2004; *Hirose*, 2006], is under debate. The recent Mössbauer spectroscopy measurements by *Jackson et al.* [2009] reported the coexistence of Fe^{3+}-dominant Al-free PPv and metallic iron. In contrast, the similar Mössbauer study by *Lin et al.* [2008] found that Al-free PPv included iron as Fe^{2+}, consistent with the earlier electron energy-loss near-edge structure (ELNES) measurements [*Sinmyo et al.*, 2008a]. Studies of $Fe^{3+}/\Sigma Fe$ ratio in Al-bearing PPv are also very limited so far [*Sinmyo et al.*, 2006; *Zhang and Oganov*, 2006].

[4] Both theory [*Caracas and Cohen*, 2008] and experiments [*Catalli et al.*, 2009; *Andrault et al.*, 2010] have suggested that Pv and PPv coexist in a wide pressure range in $MgSiO_3$-$FeSiO_3$ binary system, corresponding to >300 km thick region for a plausible iron content (e.g., 10 mol% $FeSiO_3$). It was therefore suggested that the D″ layer is a mixed phase region and the abrupt shear wave velocity jump at the D″ discontinuity is of a chemical origin [*Catalli et al.*, 2009; *Andrault et al.*, 2010]. Nevertheless, the $Fe^{3+}/\Sigma Fe$ ratio in Al-bearing PPv might control the Fe partitioning between PPv and Fp, which affects the pressure range for Pv + PPv two-phase loop or the phase equilibria conditions for the Pv-PPv transition.

[5] In this study, we synthesized Al-bearing Pv and PPv at high pressure and temperature (*P*-*T*) using laser-heated diamond-anvil cell (DAC) techniques. The $Fe^{3+}/\Sigma Fe$ ratios in such Pv and PPv were subsequently determined on

[1]Department of Earth and Planetary Sciences, Tokyo Institute of Technology, Tokyo, Japan.
[2]Now at Bayerisches Geoinstitut, Universität Bayreuth, Bayreuth, Germany.
[3]Institute for Research on Earth Evolution, Japan Agency for Marine-Earth Science and Technology, Kanagawa, Japan.
[4]Nagoya University, Nagoya, Japan.
[5]Japan Synchrotron Radiation Research Institute, Sayo, Japan.
[6]JEOL Ltd., Tokyo, Japan.

0148-0227/11/2010JB008179

Table 1. Experimental Conditions and Results[a]

Starting Material and Run	Pressure (GPa)	Temperature (K)	Phase	$Fe^{3+}/\Sigma Fe$	Total Fe*O[b] (wt %)	Al_2O_3 (wt %)
Fe^{2+}-Dominant Starting Material						
$(Mg_{0.84}Fe_{0.10})(Al_{0.10}Si_{0.96})O_3$			SM	0.04(3)	6.6	5.0
NO61	61	2200	Pv	0.51(7)	6.7(5)	4.8(8)
NO146	146	1900	PPv	0.23(3)	6.6(3)	5.2(4)
$(Mg_{0.79}Fe_{0.11})(Al_{0.16}Si_{0.94})O_3$			SM	0.07(5)	7.6	7.9
SO44	44	2400	Pv	0.80(15)	5.7(10)	7.0(6)
SO149	149	3500	PPv	0.11(11)	7.3(8)	6.9(9)
$(Mg_{0.79}Fe_{0.08})(Al_{0.22}Si_{0.91})O_3$			SM	0.22(6)	4.9	10.4
SG155	155	3400	PPv	0.19(10)	4.5(11)	9.6(7)
Pyrolitic mantle (KLB-1 peridotite)[c]			SM	0.22(13)		
PY93	93	2300	Pv	0.59(12)	7.7(4)	4.8(6)
PY135	135	2400	PPv	0.21(13)	2.5(8)	4.1(12)
Oxidized Starting Material						
$(Mg_{0.79}Fe_{0.08})(Al_{0.22}Si_{0.91})O_3$			SM	0.50(11)	4.9	10.4
SGM146	146	2300	PPv	0.45(11)	5.5(4)	9.7(7)
$(Mg_{0.79}Fe_{0.08})(Al_{0.22}Si_{0.91})O_3$			SM	0.57(12)	4.9	10.4
SGH143	143	2400	PPv	0.46(9)	5.8(12)	10.0(1)

[a]Numbers in parentheses indicate errors (SD) in the last digits. SM, starting material.
[b]Total Fe as FeO.
[c]The weight percents are 45.8 wt % SiO_2, 4.0 wt % Al_2O_3, 8.2 wt % FeO, 38.1 wt % MgO, and 3.9 wt % CaO.

recovered samples on the basis of ELNES spectroscopy measurements under transmission electron microscope (TEM). The results indicate that the $Fe^{3+}/\Sigma Fe$ ratio in Pv increases with increasing Al^{3+} content also at deep lower mantle conditions, consistent with the previous multianvil experiments performed at relatively low pressures [e.g., *McCammon*, 1997; *Lauterbach et al.*, 2000; *Frost and Langenhorst*, 2002]. On the other hand, PPv includes iron predominantly as Fe^{2+} even when the Al^{3+} content is high. It suggests that the valence state of iron dramatically changes across the perovskite to postperovskite phase transition. This has profound implications for Fe partitioning, phase transition, and elastic/transport properties in the lowermost mantle. The phase transition between Pv and Fe-poor PPv occurs in much narrower pressure range than for isochemical transition.

2. Experiments

2.1. Starting Materials

[6] We prepared a total of six starting materials with mainly changing Al_2O_3 content and $Fe^{3+}/\Sigma Fe$ ratio (Table 1). Natural $(Mg_{0.84}Fe_{0.10})(Al_{0.10}Si_{0.96})O_3$ orthopyroxene was taken from the KLB-1 peridotite [*Takahashi*, 1986]. $(Mg_{0.79}Fe_{0.11})(Al_{0.16}Si_{0.94})O_3$ and $(Mg_{0.79}Fe_{0.08})(Al_{0.22}Si_{0.91})O_3$ orthopyroxenes were synthesized from oxides and gel, respectively, at 1 GPa and 1473 K in a piston-cylinder apparatus. Their chemical homogeneity was confirmed by microprobe analyses. We prepared pyrolitic mantle material originally as gel with a chemical composition of natural KLB-1 peridotite [*Murakami et al.*, 2005; *Ohta et al.*, 2008]. The gels were dehydrated at 1000 K in a H_2-CO_2 gas-mixing furnace, in which oxygen fugacity was controlled slightly above the iron-wüstite buffer. These four starting materials have low $Fe^{3+}/\Sigma Fe$ ratios of 0.04–0.22. Additionally, a couple of oxidized $(Mg_{0.79}Fe_{0.08})(Al_{0.22}Si_{0.91})O_3$ samples were prepared by modifying the $Fe^{3+}/\Sigma Fe$ ratio to be 0.50 and 0.57 in the gas-mixing furnace.

2.2. High-Pressure Experiments

[7] Three Pv and six PPv samples were synthesized at high *P-T* using laser-heated DAC techniques at the beam line BL10XU of SPring-8. Details of experiments are summarized in Table 2. In order to avoid strong temperature gradient, which causes chemical segregation [*Sinmyo and Hirose*, 2010] and Fe-metal forming reaction [*Fialin et al.*, 2008], the sample was not mixed with a metal powder but coated with gold for both sides (0.2 to 2 μm thickness) [*Sinmyo and Hirose*, 2010], except in run SG155 in which no additional laser absorber was used. It was then loaded into a hole drilled in preindented Re gasket together with insulation layers of SiO_2 glass. After compression at 300 K, the sample was heated from both sides by a multimode neodymium: yttrium/aluminum/garnet (Nd:YAG) laser or a fiber laser. Temperature was measured by the spectroradiometric method [see *Sinmyo and Hirose*, 2010, Figure 2c]. Pressure was estimated from the Raman spectrum of diamond [*Akahama and Kawamura*, 2004] at room temperature after heating. Errors of estimated pressure should be smaller than ±10% [*Akahama and Kawamura*, 2004]. Synchrotron X-ray diffraction (XRD) measurements were conducted for phase identification (Figure 1).

2.3. TEM Analysis

[8] The samples were recovered from the DAC and subsequently Ar ion thinned by the Ion Slicer [*Tateno et al.*, 2009a]. Selected samples were chemically analyzed by a field-emission-type electron microprobe analyzer (FE-EPMA) to obtain x-ray maps. After that, thin sections were further Ar ion thinned for the examination by TEM (Figure 2). We measured major elements by energy-dispersive X-ray spectroscopy (EDS) using *k* factors [*Cliff and Lorimer*, 1975], which were determined using natural alkali-basalt glass as standard. The analyses of several microns areas using defocused beam indicated that the sample preserved original bulk composition. $Fe^{3+}/\Sigma Fe$ ratios in Pv and PPv were determined by the Fe $L_{2,3}$-edge ELNES spectroscopy mea-

Table 2. Details of Experiments

Starting Material and Run	Phase	P (GPa)	T (K)	Duration (min)	Laser[a]	Laser Absorber	Pressure Medium	ELNES Measurement[b]
$(Mg_{0.84}Fe_{0.10})(Al_{0.10}Si_{0.96})O_3$								1
NO61	Pv	61	2200	60	Nd:YAG	Coating (2 μm gold)	SiO_2 glass	1
NO146	PPv	146	1900	120	Fiber	Coating (2 μm gold)	SiO_2 glass	1
$(Mg_{0.79}Fe_{0.11})(Al_{0.16}Si_{0.94})O_3$								1, 2
SO44	Pv	44	2400	60	Nd:YAG	Coating (0.2 μm gold)	SiO_2 glass	2
SO149	PPv	149	3500	30	Fiber	Coating (0.2 μm gold)	SiO_2 glass	3
$(Mg_{0.79}Fe_{0.08})(Al_{0.22}Si_{0.91})O_3$								2, 3
SG155	PPv	155	3400	60	Fiber	None	SiO_2 glass	3
$(Mg_{0.79}Fe_{0.08})(Al_{0.22}Si_{0.91})O_3$								3
SGM146	PPv	146	2300	60	Fiber	Coating (1 μm gold)	SiO_2 glass	3
$(Mg_{0.79}Fe_{0.08})(Al_{0.22}Si_{0.91})O_3$								3
SGH143	PPv	143	2400	60	Fiber	Coating (1 μm gold)	SiO_2 glass	3
Pyrolite (KLB-1 Peridotite)								3
PY93	Pv	93	2300	60	Fiber	Coating (1 μm gold)	SiO_2 glass	3
PY135	PPv	135	2400	60	Fiber	Coating (1 μm gold)	SiO_2 glass	3

[a]ND:YAG, neodymium:yttrium/aluminum/garnet.
[b]The ELNES measurements are 1, JEM-2100F + Enfina1000; 2, JEM-2100M + Enfina1000; 3, JEM-2100F + GIF-Tridiem.

surements (Figure 3), similarly to the previous studies [*Lauterbach et al.*, 2000; *Frost and Langenhorst*, 2002; *Frost et al.*, 2004; *Sinmyo et al.*, 2006, 2008a; *Irifune et al.*, 2010]. The ELNES spectroscopy measurements cannot be performed in situ at high pressure but have quite high spatial resolution (~10 nm scale) compared to that of Mössbauer spectroscopy (several μm scale) [e.g., *McCammon et al.*, 2004; *Jackson et al.*, 2009]. Therefore, the ELNES spectroscopy has the advantage over the Mössbauer spectroscopy for samples containing multiple iron-bearing phases such as pyrolitic material.

[9] We obtained the spectra by using field-emission-type JEM-2100F with GATAN Enfina1000 spectrometer or GIF-Tridiem energy filter at the JEOL Ltd. or using JEM-2100M with Enfina1000 spectrometer at the Nagoya University (Table 2). Four to eight areas were analyzed in each sample with electron beam size of 50 nm to 1 μm. We examined very thin part but avoided very edge of the sample, which was possibly damaged by Ar ion beam. The measurements were made with dispersion of 0.1 eV per channel, typical energy resolution of about 0.8 eV, and integration time of 5–60 s for JEM-2100F and 10–60 s for JEM-2100M. For JEM-2100M, the spectra were recorded using a macroscript for Gatan Digital Micrograph™ to control the spectrometer that corrects for energy drifts during data accumulation. This ensures to avoid peak broadening by prolonged data accumulation [*Sasano and Muto*,

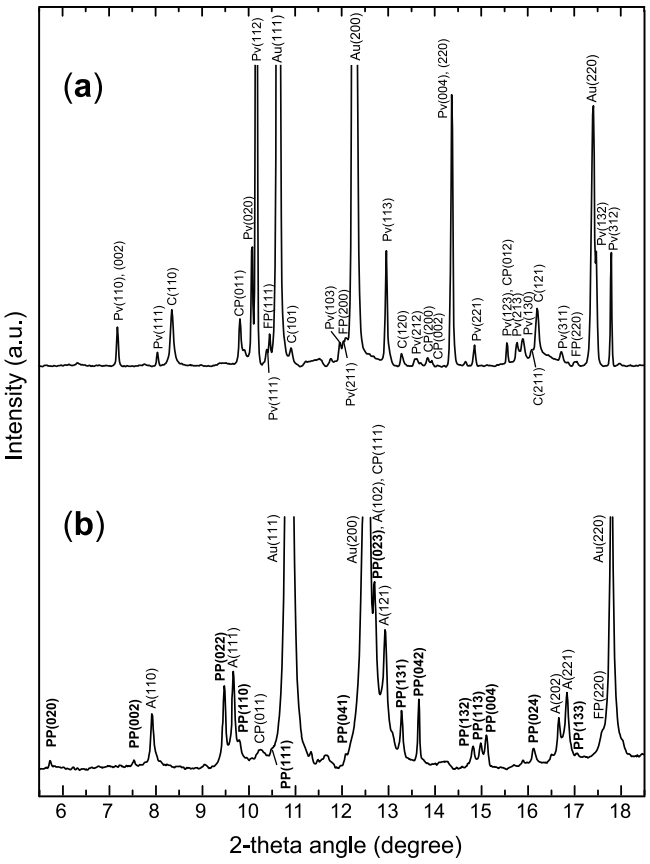

Figure 1. X-ray diffraction (XRD) patterns of pyrolitic mantle material at (a) 93 GPa and (b) 135 GPa. Note that the sample was separated from the SiO_2 pressure medium by gold layers in between. Pv, perovskite; PP, postperovskite; FP, ferropericlase; CP, $CaSiO_3$-rich perovskite; C, $CaCl_2$-type SiO_2; A, α-PbO_2-type SiO_2; Au, gold.

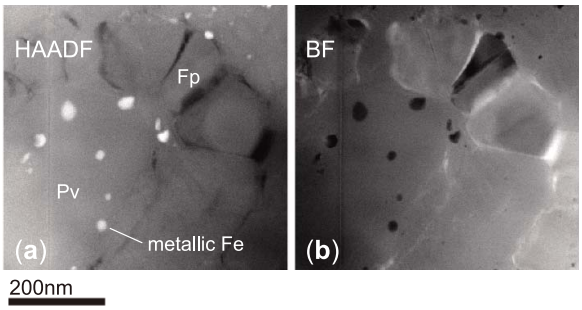

Figure 2. Transmission electron microscope (TEM) images showing the coexistence of Pv and metallic particles obtained in run PY93: (a) high-angle annular dark-field (HAADF) scanning TEM image and (b) bright field (BF) image.

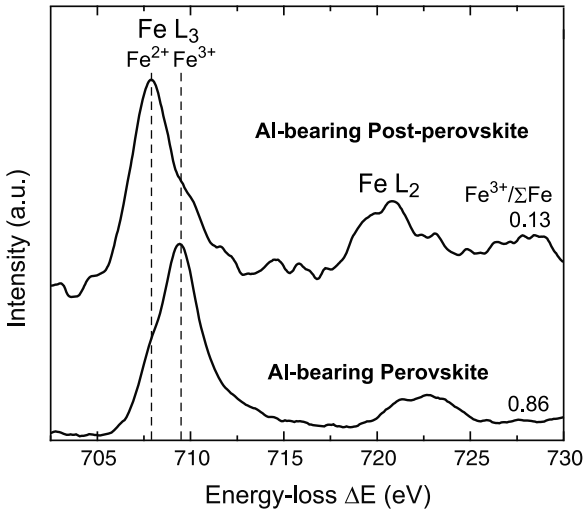

Figure 3. Typical ELNES spectra of (Al, Fe)-bearing Pv and PPv. Fe $L_{2,3}$-edge spectra of Pv (SO44) and PPv (SO149).

2008]. The incident beam current was about 0.1 nA, and the fluence rate was about 70 e/Å^2/sec for JEM-2100F and 50 e/Å^2/sec for JEM-2100M. The spectra were corrected for dark current and channel-to-channel gain variation of the detector, and the inverse power law background was subtracted. The quantitative determination of the $Fe^{3+}/\Sigma Fe$ ratio is based on the white line intensities at the Fe $L_{2,3}$-edge, following the method described by *van Aken et al.* [1998]. The validity of the present analytical procedures was checked on a couple of silicate glass standards, whose $Fe^{3+}/\Sigma Fe$ ratios were previously determined by the Mössbauer spectroscopy measurements to be 0.38 and 0.83 [*Jayasuriya et al.*, 2004]. Our ELNES analyses provided the $Fe^{3+}/\Sigma Fe$ ratios for these glass samples to be 0.29 ± 0.04 and 0.81 ± 0.04 by JEM-2100F with Enfina1000, 0.34 ± 0.11 and 0.80 ± 0.04 by JEM-2100F with GIF-Tridiem, and 0.40 ± 0.02 and 0.79 ± 0.09 by JEM-2100M. These values are in good agreement with the Mössbauer analyses, considering the intrinsic uncertainty in the EELS measurements (about ±0.1) [*Lauterbach et al.*, 2000]. Note that these standard glass samples were Ar ion thinned following the same procedure as that used for high-pressure samples. In addition, the results of time series measurements obtained for Pv and PPv samples with JEM-2100F indicate that the measured $Fe^{3+}/\Sigma Fe$ ratios did not change with increasing electron beam irradiation time up to 60 s (Figure 4).

[10] The $Fe^{3+}/\Sigma Fe$ ratios were determined also for all the starting materials used in this study. The orthopyroxene starting materials were Ar ion thinned by the Ion Slicer in the same way. For the gel starting materials, we analyzed the unheated part of the DAC samples to obtain their $Fe^{3+}/\Sigma Fe$ ratios.

3. Results

[11] Synchrotron XRD measurements performed at high pressure demonstrated that the sample was single phase Pv or PPv when using the orthopyroxene as a starting material (run series of NO, SO, SG, SGM and SGH). X-ray mappings obtained by FE-EPMA show that these samples were chemically homogeneous after heating [see *Sinmyo and Hirose*, 2010, Figure 2c]. Subsequent EDS analyses confirmed that their chemical composition was nearly identical to that of the starting material (Table 1). On the other hand, the pyrolitic material consisted predominantly of Pv (PY93) or PPv (PY135) but coexisted with minor Fp and $CaSiO_3$ perovskite (Figure 1). Major element compositions of Pv, PPv, and Fp that appeared in pyrolite are given in Table 3. In experiments using oxidized starting materials, the XRD patterns showed no extra peaks other than those from PPv, Au laser absorber, and SiO_2 pressure medium.

[12] $Fe^{3+}/\Sigma Fe$ ratios of Pv and PPv were obtained by ELNES spectroscopy measurements under the TEM (Figure 3) and plotted as a function of Al^{3+} content in Figure 5. We obtained the $Fe^{3+}/\Sigma Fe$ ratios to be 0.51 to 0.80 for Al-bearing Pv at 44 to 93 GPa (Table 1), much higher than those of the starting materials (<0.22) (Figure 6). The Pv sample was partly amorphous, but we obtained similar $Fe^{3+}/\Sigma Fe$ ratios from crystalline and amorphous parts. Amorphization of Pv likely occurred during Ar ion thinning. The $Fe^{3+}/\Sigma Fe$ ratios of Pv increased with increasing Al^{3+} content at 44–93 GPa in this study, which is in very good agreement with the previous experiments performed around 25 GPa (Figure 5) [*Lauterbach et al.*, 2000; *Frost and Langenhorst*, 2002]. These Pv samples coexisted with metallic iron as shown in the TEM image (Figure 2).

[13] In contrast to the Pv samples, metallic iron was not observed in the PPv samples. The measured $Fe^{3+}/\Sigma Fe$ ratios were low for PPv, ranging from 0.11 to 0.23, when using Fe^{3+}-poor starting materials ($Fe^{3+}/\Sigma Fe < 0.22$) (Table 1). Note that the $Fe^{3+}/\Sigma Fe$ ratio in PPv is independent from the Al^{3+} content (Figure 5). On the other hand, it is controlled by the $Fe^{3+}/\Sigma Fe$ ratio in starting material. In this study, the PPv samples were synthesized also from oxidized starting materials with elevated $Fe^{3+}/\Sigma Fe$ ratios of 0.50 and 0.57 (Table 1). The $Fe^{3+}/\Sigma Fe$ ratios in such PPv were indeed

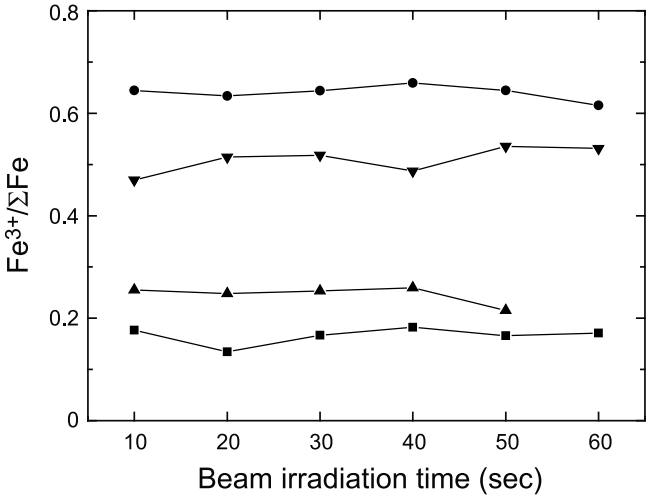

Figure 4. Variations in measured $Fe^{3+}/\Sigma Fe$ ratio with increasing beam irradiation time. Squares, PPv (PY135); triangles, PPv (SO149); inverse triangles, Pv (PY93); circles, Pv (SO44).

Table 3. Chemical Compositions (wt %) of Coexisting Phases in Two Pyrolite-Type Materials[a]

	PY93		PY135	
	Pv	Fp	PPv	Fp
SiO_2	53.0 (27)	1.6 (8)	58.8 (28)	2.4 (5)
Al_2O_3	4.8 (6)	-	4.1 (12)	-
Fe*O[b]	7.7 (4)	17.4 (24)	2.5 (8)	24.3 (31)
FeO	3.1 (2)	17.4 (24)	2.0 (8)	24.3 (31)
Fe_2O_3	5.0 (10)	-	0.6 (4)	-
MgO	32.3 (26)	81.0 (23)	34.6 (29)	73.3 (66)
CaO	1.0 (10)	-	-	-
Mg #[c]	88.2	89.2	96.1	84.3

[a]Numbers in parentheses indicate errors in the last digits.
[b]Total Fe as FeO.
[c]Mg # is 100 × Mg/(Mg + Fe*) in molar ratio.

high (0.45 and 0.46), again similar to the values of their starting materials (Figure 6).

4. Discussion

4.1. Valence State of Iron in Pv and PPv

[14] Previous experimental studies on Pv using multianvil apparatus have demonstrated that the $Fe^{3+}/\Sigma Fe$ ratio increases with increasing Al^{3+} content [*Lauterbach et al.*, 2000; *Frost and Langenhorst*, 2002; *Frost et al.*, 2004]. Fe^{3+} in Pv can be formed concurrently with Fe metal by a valence disproportionation reaction of Fe^{2+} in the starting material ($3Fe^{2+} \rightarrow 2Fe^{3+} + Fe^0_{metal}$) [*McCammon*, 1997; *Frost et al.*, 2004]. The Al-bearing Fe^{3+}-rich Pv should thus coexist with free iron metal phase in the lower mantle [*Frost et al.*, 2004], preserving the bulk oxygen content same as that in other layers of the mantle. Our results obtained at 44–93 GPa are in good agreement with the multianvil experiments performed around 25 GPa (Figure 5), further suggesting that the Fe^{3+}–Al^{3+} coupled substitutions ($Fe^{3+} + Al^{3+} \rightarrow Fe_{Mg\text{-}site} + Al_{Si\text{-}site}$) are favored in Pv also in the deep lower mantle conditions.

[15] In contrast, similar Fe^{3+} concentrations in PPv and the starting materials strongly suggest that iron disproportionation reaction did not occur (Figure 6), which is consistent with our TEM observations that metallic phase did not coexist with PPv. It supports that amorphization of the PPv sample during decompression is not likely to have caused remarkable difference in $Fe^{3+}/\Sigma Fe$ ratio from the Pv sample. Note that the $Fe^{3+}/\Sigma Fe$ ratios are not variable with increasing Al_2O_3 content from 0 to 10 wt % in PPv [*Sinmyo et al.*, 2008a] (Figure 5). These results indicate that the Fe^{3+}–Al^{3+} coupled substitutions are not a primary mechanism of Fe and Al substitutions in PPv.

[16] The low $Fe^{3+}/\Sigma Fe$ ratio in PPv contradicts some previous experimental studies. Our preceding ELNES study [*Sinmyo et al.*, 2006] reported the high $Fe^{3+}/\Sigma Fe$ ratio of 0.65 in PPv synthesized in a natural mid-ocean ridge basalt (MORB) composition. Nevertheless, such PPv grains in MORB contained exceedingly high Na^+ (8.7 mol%) together with 11.2 mol% Fe^{3+}. The high Na^+ content likely requires specific incorporation mechanism such as Na^+–Fe^{3+} coupled substitutions ($Na^+ + Fe^{3+} = 2\ Mg^{2+}$) in PPv, which leads to the observed high $Fe^{3+}/\Sigma Fe$ ratio. Alternatively, the thin foil of this MORB sample was originally prepared for the EDS analyses [*Hirose et al.*, 2005]. It may have been oxidized over a period of more than a year before the following ELNES measurement. In the present study, the samples were Ar ion thinned right before the ELNES analyses in order to avoid such oxidation. Additionally, the previous study by *Jackson et al.* [2009] reported a coexistence of Fe^{3+}-dominant Al-free PPv and metallic iron. On the contrary, *Lin et al.* [2008] found that Al-free PPv included iron as Fe^{2+}, consistent with our ELNES measurements [*Sinmyo et al.*, 2008a]. Presence of metallic Fe in the work of *Jackson et al.* [2009] was possibly due to strong temperature gradient in laser-heated sample, which is known to cause disproportionation of ferrous iron ($3Fe^{2+} \rightarrow 2Fe^{3+} + Fe^0_{metal}$) [*Fialin et al.*, 2008].

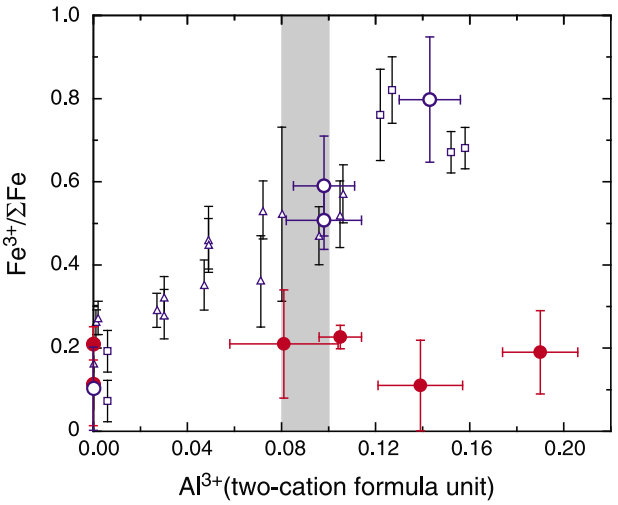

Figure 5. $Fe^{3+}/\Sigma Fe$ ratio versus Al^{3+} content in Pv and PPv, where blue open circles are for Pv and red solid circles are for PPv. Data for Al-free Pv and PPv are from *Sinmyo et al.* [2008a]. Previous experimental results on Pv obtained around 25 GPa are also shown as triangles [*Lauterbach et al.*, 2000] and squares [*Frost and Langenhorst*, 2002]. Gray indicates a plausible range of Al_2O_3 content in Pv and PPv in pyrolitic mantle [*Frost et al.*, 2004; *Murakami et al.*, 2005]. Error bars indicate 1σ.

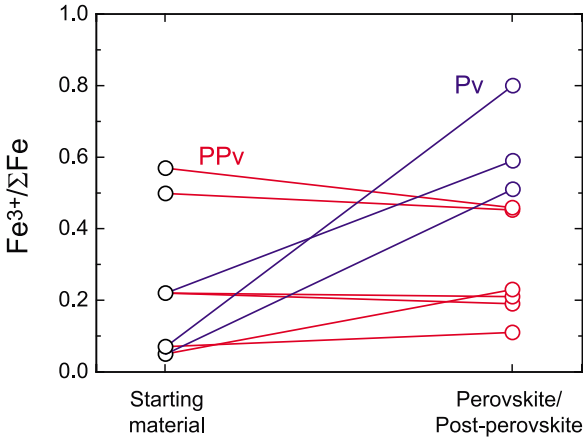

Figure 6. Comparison of $Fe^{3+}/\Sigma Fe$ ratios of Pv and PPv with those of their starting materials (Table 1). Black, starting material; blue, Pv; red, PPv.

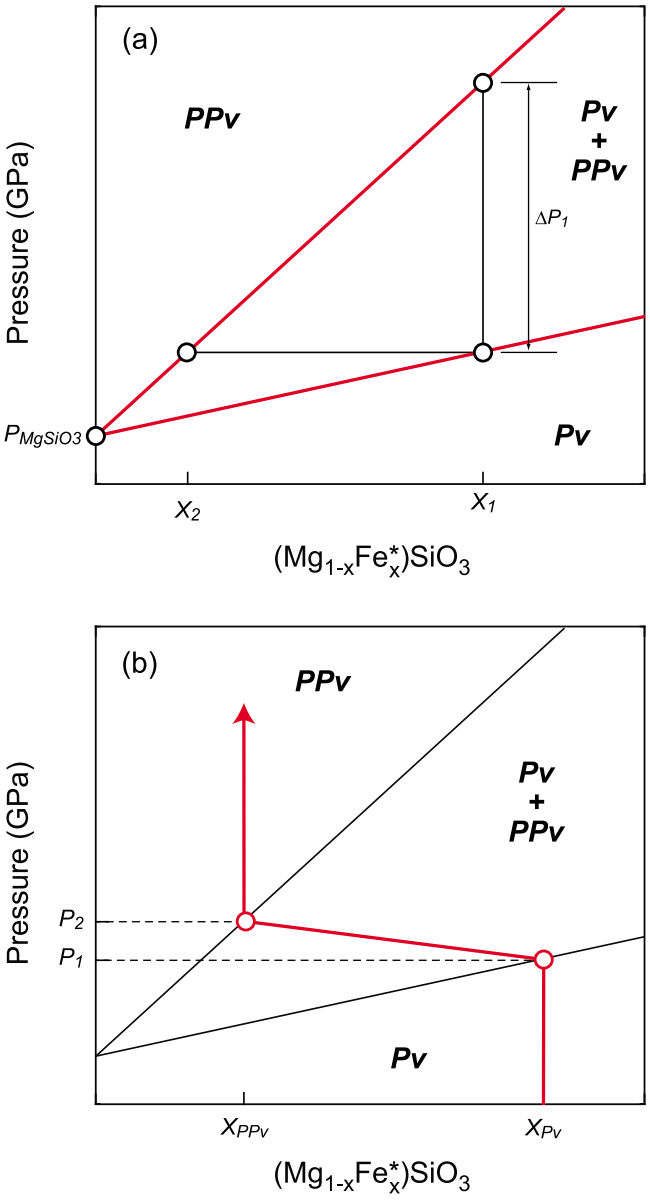

Figure 7. Schematic illustration of Pv-PPv transition in $MgSiO_3$-Fe*SiO_3 binary system, describing (a) PPv-in and Pv-out lines and (b) iron content in Pv and PPv coexisting with Fp in pyrolite. See section 4.3.

[17] While the effect of oxygen fugacity on the $Fe^{3+}/\Sigma Fe$ ratio of Al-bearing Pv has been demonstrated to be small [*Frost et al.*, 2004], it is not known for PPv. In this study, we have therefore conducted experiments with changing $Fe^{3+}/\Sigma Fe$ ratio in the starting materials from 0.04 to 0.57 (Table 1). The results indicate that the $Fe^{3+}/\Sigma Fe$ ratios in PPv samples were very similar to those of the starting materials (Figure 6). The Fe^{3+} content in PPv thus depends strongly on the abundance of oxygen available in the system, or in other words oxygen fugacity.

4.2. Effect of Iron on Stabilities of Pv and PPv

[18] The effect of iron on the stabilities of Pv and PPv has been highly controversial. Present experiments demonstrate that PPv contains much less iron than Pv in pyrolite (Table 3), suggesting that iron expands the stability field of Pv relative to PPv. This is consistent with the most recent experimental work performed by *Andrault et al.* [2010], which reported the strong Fe enrichment in Pv rather than in coexisting PPv. On the basis of the XANES measurements, *Andrault et al.* [2010] demonstrated the Fe*-Mg distribution coefficient between Pv and PPv,

$$K_{Fe*}^{Pv/PPv} = \left(X_{Fe*}^{Pv}/X_{Mg}^{Pv}\right)/\left(X_{Fe*}^{PPv}/X_{Mg}^{PPv}\right), \quad (1)$$

to be 4.2, where Fe* indicates total Fe. In the present study, our data show $K_{Fe*}^{Pv/PPv} = 5.0$ from $K_{Fe*}^{Pv/Fp} = 1.11$ at 93 GPa and $K_{Fe*}^{PPv/Fp} = 0.22$ at 135 GPa, close to the value of *Andrault et al.* [2010]. Similarly, the Fe^{2+}-Mg partition coefficient between Pv and PPv is estimated to be $K_{Fe2+}^{Pv/PPv} = 2.68$ from $K_{Fe2+}^{Pv/Fp} = 0.46$ and $K_{Fe2+}^{PPv/Fp} = 0.17$. This value is in good agreement with recent TEM work by *Hirose et al.* [2008], in which Fe-rich Pv coexisted with Fe-poor PPv in $(Mg_{0.91}Fe_{0.09})SiO_3$ bulk composition. These results are also consistent with earlier TEM observations [*Murakami et al.*, 2005] and phase equilibria study [*Tateno et al.*, 2007]. Furthermore, the very recent XRD study by *Catalli et al.* [2009] argued oppositely that iron stabilizes PPv, but their experimental results about XRD measurements themselves show that the PPv phase transition occurred in $(Mg_{0.91}Fe_{0.09})SiO_3$ at pressures higher than in pure $MgSiO_3$ (see Figure 2a in the paper by *Catalli et al.* [2009]).

[19] On the other hand, theory has predicted that the PPv structure is stable with respect to Pv in $FeSiO_3$ end-member at all pressures in the Earth's mantle [*Caracas and Cohen*, 2005; *Ono and Oganov*, 2005; *Stackhouse et al.*, 2006]. Such prediction was supported by several experimental studies [*Kobayashi et al.*, 2005; *Mao et al.*, 2007; *Auzende et al.*, 2008]. The discrepancy may be attributed to (1) the difficulty in calculating for Fe-bearing systems, (2) possible chemical segregation of Fe in laser-heated sample due to Soret effect [*Sinmyo and Hirose*, 2010], (3) disproportionation of ferrous iron into ferric and metallic Fe under strong temperature gradient [*Fialin et al.*, 2008], (4) uncertainty in pressure determination, etc.

4.3. Implications for the Lowermost Mantle

[20] Our results show that PPv contains iron predominantly as Fe^{2+} (~80%) in a pyrolitic mantle, in marked contrast to Pv which includes ca. 40% Fe^{2+} and 60% Fe^{3+} (Figure 5). Such a drastic change in the valence state of iron across the Pv to PPv transition has broad implications for properties and thereby dynamics in the lowermost mantle. While the effect of Fe^{3+} on the properties of Pv has been stressed [*Wood and Rubie*, 1996; *Xu et al.*, 1998; *Andrault et al.*, 2001; *Litasov et al.*, 2003; *McCammon*, 2005; *Goncharov et al.*, 2008; *Catalli et al.*, 2010], it does not hold for PPv. For instance, theory predicted that Fe^{3+} reduces the seismic wave velocities of PPv approximately twice as much as Fe^{2+} [*Stackhouse and Brodholt*, 2008], but in fact the role of Fe^{3+} is minor in PPv.

[21] The valence state of iron strongly affects Fe partitioning between Pv (or PPv) and coexisting Fp. PPv incorporates minimal Fe^{3+} when bulk $Fe^{3+}/\Sigma Fe$ ratio is low in the system (<0.05 in a pyrolitic mantle composition [*McCammon*,

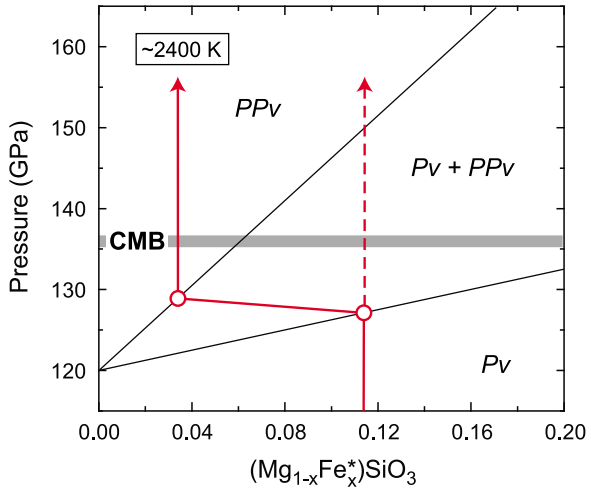

Figure 8. Schematic phase diagram in $MgSiO_3$–Fe^*SiO_3 binary system at 2400 K, demonstrating the thickness of Pv + PPv two-phase coexisting region. Fe* indicates either Fe^{2+} or Fe^{3+}, assuming that both have a similar effect on the stabilities of Pv and PPv. See section 4.3 for details. Note that the thickness of the two-phase coexisting region is much narrower when iron content decreases across the phase transition from Pv to PPv (solid arrow) than for a fixed Fe content (dashed arrow). CMB, core-mantle boundary.

2005]). Also, Fp contains iron primarily as Fe^{2+}. These indicate that iron is present predominantly as Fe^{2+} in the lowermost mantle, which consists of PPv + Fp with minor amount of $CaSiO_3$ perovskite. Upon phase transition from Pv to PPv, Fe^{3+} in Pv and metallic iron should therefore recombine to form Fe^{2+} ($2Fe^{3+}_{Pv} + Fe^{0}_{metal} \rightarrow 3Fe^{2+}$). Such proportionation reaction leads to strong iron enrichment in Fp [*Murakami et al.*, 2005], since Fe^{2+} partitions preferentially into Fp relative to Pv and PPv [*Kobayashi et al.*, 2005; *Auzende et al.*, 2008; *Sinmyo et al.*, 2008b]. Conversely PPv is depleted in iron compared to Pv [*Murakami et al.*, 2005; *Andrault et al.*, 2010]. Indeed, present experiments on pyrolite showed that PPv had only 2.5 wt % Fe*O (total Fe as FeO), much less than 7.7 wt % in Pv at 93 GPa, while Fe*O content in Fp increased from 17 to 24 wt % (Table 3). This is not likely owing to the effect of spin transition in Fp [*Badro et al.*, 2003], which changes the Fe partitioning around 40 GPa [*Irifune et al.*, 2010].

[22] Both theory [*Caracas and Cohen*, 2008] and experiments [*Catalli et al.*, 2009; *Andrault et al.*, 2010] suggested that both Pv and PPv coexist in a wide pressure range in $MgSiO_3$-$FeSiO_3$ binary system, corresponding to >300 km thick region for a plausible iron content (e.g., 10 mol% $FeSiO_3$). It was therefore suggested that the lowermost mantle, called D″ layer, is a mixed phase region and the abrupt shear wave velocity jump at the D″ discontinuity is of a chemical origin [*Catalli et al.*, 2009; *Andrault et al.*, 2010]. Nevertheless, the change in iron content across the phase transition due to partitioning between coexisting minerals controls the thickness of the boundary. For instance, the boundary between olivine and modified spinel is indeed much sharper when coexisting with majorite garnet in pyrolitic mantle composition than for a fixed Fe content [*Irifune and Isshiki*, 1998].

[23] Figure 7 is a schematic phase diagram demonstrating how the change in iron content affects the width of the Pv to PPv phase transition. Here we consider that iron stabilizes Pv relative to PPv (see section 4.2) and that iron partition coefficient is constant with changing bulk iron content. Both PPv-in and Pv-out lines in Figure 7a can be drawn from (1) transition pressure in pure $MgSiO_3$ (P_{MgSiO3}), (2) width of Pv + PPv coexisting field (ΔP_1) for a given Fe content (X_1), and (3) Fe*-Mg distribution coefficient between Pv and PPv ($K_{Fe^*}^{Pv/PPv}$) that determines iron content X_2 ($= X_1/K_{Fe^*}^{Pv/PPv}$) in PPv coexisting with Pv with X_1 iron content. The width of the phase transition ($P_2 - P_1$) can be obtained as

$$(P_2 - P_1) = \Delta P_1 \times \left(K_{Fe^*}^{Pv/PPv} \times X_{PPv} - X_{Pv}\right) / \left(K_{Fe^*}^{Pv/PPv} - 1\right) / X_1, \quad (2)$$

where X_{Pv} and X_{PPv} are iron content in Pv and PPv coexisting with Fp in pyrolitic bulk composition before and after the phase transition (Figure 7b).

[24] Pressure of Pv–PPv transition has been determined to be 120 GPa at 2400 K [*Tateno et al.*, 2009b]. *Catalli et al.* [2009] reported the pressure range of 20 GPa for Pv + PPv mixed region in $(Mg_{0.91}Fe_{0.09})SiO_3$. *Andrault et al.* [2010] showed the Fe*-Mg distribution coefficient between Pv and PPv, $K_{Fe^*}^{Pv/PPv}$ to be 4.2, close to our data. Pv and PPv formed in pyrolitic mantle material in this study exhibit the Fe*/(Mg + Fe*) molar ratios of 0.12 and 0.04, respectively (Table 3). On the basis of these experimental data, we draw a schematic phase diagram in $MgSiO_3$–Fe^*SiO_3 binary system at 2400 K (Figure 8). Here we assume that Fe^{2+} and Fe^{3+} have similar effect on the stabilities of Pv and PPv, although previous experiments by *Catalli et al.* [2009] demonstrated that Fe^{3+} has smaller effect on expanding the width of the PPv transition. Figure 8 illustrates that the phase transition from Pv to Fe-poor PPv occurs in about 3 GPa, consistent with the sharpness of the boundary determined by the previous phase equilibria study on pyrolite [*Ohta et al.*, 2008]. Note that this is much sharper than for a fixed FeO content (about 20 GPa for $(Mg_{0.91}Fe_{0.09})SiO_3$) [*Catalli et al.*, 2009]. The observed shear velocity jump at the D″ discontinuity is therefore reconciled with the PPv phase transition in the presence of Fp in pyrolitic mantle material, although the effect of Al_2O_3 impurity remains to be examined.

[25] **Acknowledgments.** We thank E. Takahashi for preparation of starting materials and T. Komabayashi for valuable comments. Review comments by two anonymous referees helped significantly in improving the manuscript. Experiments were carried out at SPring-8 (proposals 2009A0087 and 2009B0087). R.S. was supported by the JSPS Research Fellowship for Young Scientists.

References

Akahama, Y., and H. Kawamura (2004), High pressure Raman spectroscopy of diamond anvils to 250 GPa: Method for pressure determination in the multimegabar pressure range, *J. Appl. Phys.*, *96*, 3748–3751, doi:10.1063/1.1778482.

Andrault, D., N. Bolfan-Casanova, and N. Guignot (2001), Equation of state of lower mantle (Al,Fe)-$MgSiO_3$ perovskite, *Earth Planet. Sci. Lett.*, *193*, 501–508, doi:10.1016/S0012-821X(01)00506-4.

Andrault, D., M. Muñoz, N. Bolfan-Casanova, N. Guignot, J.-P. Perrillat, G. Aquilanti, and S. Pascarelli (2010), Experimental evidence for perovskite and post-perovskite coexistence throughout the whole D″ region, *Earth Planet. Sci. Lett.*, *293*, 90–96, doi:10.1016/j.epsl.2010.02.026.

Auzende, A. L., J. Badro, F. J. Ryerson, P. K. Weber, S. J. Fallon, A. Addad, J. Siebert, and G. Fiquet (2008), Element partitioning between magnesium silicate perovskite and ferropericlase: New insights into bulk lower-mantle geochemistry, *Earth Planet. Sci. Lett.*, *269*, 164–174, doi:10.1016/j.epsl.2008.02.001.

Badro, J., G. Fiquet, F. Guyot, J.-P. Rueff, V. V. Struzhkin, G. Vankó, and G. Monaco (2003), Iron partitioning in Earth's mantle: Toward a deep lower mantle discontinuity, *Science*, *300*, 789–791, doi:10.1126/science.1081311.

Caracas, R., and R. E. Cohen (2005), Effect of chemistry on the stability and elasticity of the perovskite and post-perovskite phases in the $MgSiO_3$-$FeSiO_3$-Al_2O_3 system and implications for the lowermost mantle, *Geophys. Res. Lett.*, *32*, L16310, doi:10.1029/2005GL023164.

Caracas, R., and R. E. Cohen (2008), Ferrous iron in post-perovskite from first-principles calculations, *Phys. Earth Planet. Inter.*, *168*, 147–152, doi:10.1016/j.pepi.2008.06.002.

Catalli, K., S. H. Shim, and V. Prakapenka (2009), Thickness and Clapeyron slope of the post-perovskite boundary, *Nature*, *462*, 782–785, doi:10.1038/nature08598.

Catalli, K., S. H. Shim, V. B. Prakapenka, J. Zhao, W. Sturhahn, P. Chow, Y. Xiao, H. Liu, H. Cynn, and W. J. Evans (2010), Spin state of ferric iron in $MgSiO_3$ perovskite and its effect on elastic properties, *Earth Planet. Sci. Lett.*, *289*, 68–75, doi:10.1016/j.epsl.2009.10.029.

Cliff, G., and G. W. Lorimer (1975), The quantitative analysis of thin specimens, *J. Microsc.*, *103*, 203–207.

Fialin, M., G. Catillon, and D. Andrault (2008), Disproportionation of Fe^{2+} in Al-free silicate perovskite in the laser heated diamond anvil cell as recorded by electron probe microanalysis of oxygen, *Phys. Chem. Miner.*, *36*, 183–191, doi:10.1007/s00269-008-0268-9.

Frost, D. J., and F. Langenhorst (2002), The effect of Al_2O_3 on Fe-Mg partitioning between magnesiowüstite and magnesium silicate perovskite, *Earth Planet. Sci. Lett.*, *199*, 227–241, doi:10.1016/S0012-821X(02)00558-7.

Frost, D. J., C. Liebske, F. Langenhorst, C. A. McCammon, R. G. Trønnes, and D. C. Rubie (2004), Experimental evidence for the existence of iron-rich metal in the Earth's lower mantle, *Nature*, *428*, 409–412, doi:10.1038/nature02413.

Goncharov, A. F., B. D. Haugen, V. V. Struzhkin, P. Beck, and S. D. Jacobsen (2008), Radiative conductivity in the Earth's lower mantle, *Nature*, *456*, 231–234, doi:10.1038/nature07412.

Hirose, K. (2006), Postperovskite phase transition and its geophysical implications, *Rev. Geophys.*, *44*, RG3001, doi:10.1029/2005RG000186.

Hirose, K., N. Takafuji, N. Sata, and Y. Ohishi (2005), Phase transition and density of subducted MORB crust in the lower mantle, *Earth Planet. Sci. Lett.*, *237*, 239–251, doi:10.1016/j.epsl.2005.06.035.

Hirose, K., N. Takafuji, K. Fujino, S. R. Shieh, and S. Duffy (2008), Iron partitioning between perovskite and post-perovskite: A transmission electron microscope study, *Am. Mineral.*, *93*, 1678–1681, doi:10.2138/am.2008.3001.

Irifune, T., and M. Isshiki (1998), Iron partitioning in a pyrolite mantle and the nature of the 410-km seismic discontinuity, *Nature*, *392*, 702–705, doi:10.1038/33663.

Irifune, T., T. Shinmei, C. A. McCammon, N. Miyajima, D. C. Rubie, and D. J. Frost (2010), Iron partitioning and density changes of pyrolite in Earth's lower mantle, *Science*, *327*, 193–195, doi:10.1126/science.1181443.

Jackson, J. M., W. Sturhahn, O. Tschauner, M. Lerche, and Y. Fei (2009), Behavior of iron in $(Mg,Fe)SiO_3$ post-perovskite assemblages at Mbar pressures, *Geophys. Res. Lett.*, *36*, L10301, doi:10.1029/2009GL037815.

Jayasuriya, K., H. S. C. O'Neill, A. J. Berry, and S. J. Campbell (2004), A Mössbauer study of the oxidation state of Fe in silicate melts, *Am. Mineral.*, *89*, 1597–1609.

Kobayashi, Y., T. Kondo, E. Ohtani, N. Hirao, N. Miyajima, T. Yagi, T. Nagase, and T. Kikegawa (2005), Fe-Mg partitioning between $(Mg, Fe)SiO_3$ post-perovskite, perovskite, and magnesiowüstite in the Earth's lower mantle, *Geophys. Res. Lett.*, *32*, L19301, doi:10.1029/2005GL023257.

Lauterbach, S., C. McCammon, P. van Aken, F. Langenhorst, and F. Seifert (2000), Mössbauer and ELNES spectroscopy of $(Mg,Fe)(Si,Al)O_3$ perovskite: A highly oxidized component of the lower mantle, *Contrib. Mineral. Petrol.*, *138*, 17–26, doi:10.1007/PL00007658.

Lin, J. F., et al. (2008), Intermediate-spin ferrous iron in lowermost mantle post-perovskite and perovskite, *Nat. Geosci.*, *1*, 688–691, doi:10.1038/ngeo310.

Litasov, K., E. Ohtani, F. Langenhorst, H. Yurimoto, T. Kubo, and T. Kondo (2003), Water solubility in Mg-perovskites and water storage capacity in the lower mantle, *Earth Planet. Sci. Lett.*, *211*, 189–203, doi:10.1016/S0012-821X(03)00200-0.

Mao, W. L., A. J. Campbell, V. B. Prakapenka, R. J. Hemley, and H. K. Mao (2007), Effect of iron on the properties of post-perovskite silicate, in *Post-Perovskite: The Last Mantle Phase Transition*, *Geophys. Monogr. Ser.*, vol. 174, edited by K. Hirose et al., pp. 37–46, AGU, Washington, D. C.

McCammon, C. (1997), Perovskite as a possible sink for ferric iron in the lower mantle, *Nature*, *387*, 694–696, doi:10.1038/42685.

McCammon, C. A. (2005), Mantle oxidation state and oxygen fugacity: Constraints on mantle chemistry, structure, and dynamics, in *Earth's Deep Mantle: Structure, Composition, and Evolution*, *Geophys. Monogr. Ser.*, vol. 160, edited by R. D. van der Hilst et al., pp. 221–242, AGU, Washington, D. C.

McCammon, C. A., S. Lauterbach, F. Seifert, F. Langenhorst, and P. A. van Aken (2004), Iron oxidation state in lower mantle mineral assemblages I. Empirical relations derived from high-pressure experiments, *Earth Planet. Sci. Lett.*, *222*, 435–449, doi:10.1016/j.epsl.2004.03.018.

Murakami, M., K. Hirose, K. Kawamura, N. Sata, and Y. Ohishi (2004), Post-perovskite phase transition in $MgSiO_3$, *Science*, *304*, 855–858, doi:10.1126/science.1095932.

Murakami, M., K. Hirose, N. Sata, and Y. Ohishi (2005), Post-perovskite phase transition and mineral chemistry in the pyrolitic lowermost mantle, *Geophys. Res. Lett.*, *32*, L03304, doi:10.1029/2004GL021956.

Oganov, A. R., and S. Ono (2004), Theoretical and experimental evidence for a post-perovskite phase of $MgSiO_3$ in Earth's D″ layer, *Nature*, *430*, 445–448, doi:10.1038/nature02701.

Ohta, K., K. Hirose, T. Lay, N. Sata, and Y. Ohishi (2008), Phase transitions in pyrolite and MORB at lowermost mantle conditions: Implications for a MORB-rich pile above the core-mantle boundary, *Earth Planet. Sci. Lett.*, *267*, 107–117, doi:10.1016/j.epsl.2007.11.037.

Ono, S., and A. R. Oganov (2005), In situ observations of phase transition between perovskite and $CaIrO_3$-type phase in $MgSiO_3$ and pyrolitic mantle composition, *Earth Planet. Sci. Lett.*, *236*, 914–932, doi:10.1016/j.epsl.2005.06.001.

Sasano, Y., and S. Muto (2008), Energy-drift correction of electron energy-loss spectra from prolonged data accumulation of low SNR signals, *J. Electron Microsc.*, *57*, 149–158, doi:10.1093/jmicro/dfn014.

Sinmyo, R., and K. Hirose (2010), The Soret diffusion in laser-heated diamond-anvil cell, *Phys. Earth Planet. Inter.*, *180*, 172–178, doi:10.1016/j.pepi.2009.10.011.

Sinmyo, R., K. Hirose, H. S. O'Neill, and E. Okunishi (2006), Ferric iron in Al-bearing post-perovskite, *Geophys. Res. Lett.*, *33*, L12S13, doi:10.1029/2006GL025858.

Sinmyo, R., H. Ozawa, K. Hirose, A. Yasuhara, N. Endo, N. Sata, and Y. Ohishi (2008a), Ferric iron content in $(Mg,Fe)SiO_3$ perovskite and post-perovskite at deep lower mantle conditions, *Am. Mineral.*, *93*, 1899–1902, doi:10.2138/am.2008.2806.

Sinmyo, R., K. Hirose, D. Nishio-Hamane, Y. Seto, K. Fujino, N. Sata, and Y. Ohishi (2008b), Partitioning of iron between perovskite/postperovskite and ferropericlase in the lower mantle, *J. Geophys. Res.*, *113*, B11204, doi:10.1029/2008JB005730.

Stackhouse, S., and J. P. Brodholt (2008), Elastic properties of the post-perovskite phase of Fe_2O_3 and implications for ultra-low velocity zones, *Phys. Earth Planet. Inter.*, *170*, 260–266, doi:10.1016/j.pepi.2008.07.010.

Stackhouse, S., J. P. Brodholt, and G. D. Price (2006), Elastic anisotropy of $FeSiO_3$ end-members of the perovskite and post-perovskite phases, *Geophys. Res. Lett.*, *33*, L01304, doi:10.1029/2005GL023887.

Takahashi, E. (1986), Melting of a dry peridotite KLB-1 up to 14 GPa: Implications on the origin of peridotitic upper mantle, *J. Geophys. Res.*, *91*, 9367–9382, doi:10.1029/JB091iB09p09367.

Tateno, S., K. Hirose, N. Sata, and Y. Ohishi (2007), Solubility of FeO in $(Mg,Fe)SiO_3$ perovskite and post-perovskite phase transition, *Phys. Earth Planet. Inter.*, *160*, 319–325, doi:10.1016/j.pepi.2006.11.010.

Tateno, S., R. Sinmyo, K. Hirose, and H. Nishioka (2009a), The advanced ion-milling method for preparation of thin film using Ion Slicer: Application to a sample recovered from diamond-anvil cell, *Rev. Sci. Instrum.*, *80*, 013901, doi:10.1063/1.3058760.

Tateno, S., K. Hirose, N. Sata, and Y. Ohishi (2009b), Determination of post-perovskite phase transition boundary up to 4400 K and implications

for thermal structure in D″ layer, *Earth Planet. Sci. Lett.*, *277*, 130–136, doi:10.1016/j.epsl.2008.10.004.

van Aken, P. A., B. Liebscher, and V. J. Styrsa (1998), Quantitative determination of iron oxidation states in minerals using Fe $L_{2,3}$-edge electron energy-loss near-edge structure spectroscopy, *Phys. Chem. Miner.*, *25*, 323–327, doi:10.1007/s002690050122.

Wood, B. J., and D. C. Rubie (1996), The effect of alumina on phase transitions at the 660-kilometer discontinuity from Fe-Mg partitioning experiments, *Science*, *273*, 1522–1524, doi:10.1126/science.273.5281.1522.

Xu, Y., C. McCammon, and B. T. Poe (1998), The effect of alumina on the electrical conductivity of silicate perovskite, *Science*, *282*, 922–924, doi:10.1126/science.282.5390.922.

Zhang, F., and A. R. Oganov (2006), Valence state and spin transition of iron in Earth's mantle silicates, *Earth Planet. Sci. Lett.*, *249*, 436–443, doi:10.1016/j.epsl.2006.07.023.

K. Hirose, Department of Earth and Planetary Sciences, Tokyo Institute of Technology, 2-12-1, Ookayama, Meguro, Tokyo 152-8551, Japan. (kei@geo.titech.ac.jp)

S. Muto, Department of Materials, Physics and Energy Engineering, Nagoya University, Nagoya 464-8603, Japan.

Y. Ohishi, Japan Synchrotron Radiation Research Institute, Mikazuki-cho, Sayo, Hyogo 679-5198, Japan.

R. Sinmyo, Bayerisches Geoinstitut, Universität Bayreuth, D-95440 Bayreuth, Germany.

A. Yasuhara, JEOL Ltd., Akishima, Tokyo 196-8558, Japan.